Supporting Information

Su et al. 10.1073/pnas.1212506109

SI Text

SI Methods. ***Preparing and incubating human sperm suspension.*** Fresh semen specimens within less than 1 h after collection (from anonymous donors) were obtained from California Cryobank without preprocessing. Only specimens with high sperm concentration ($>50 \times 10^6$ sperms per mL) and high motility (>70% motile) were used in our experiments. The motile sperms were first separated from seminal plasma by centrifugation with density gradient media (ISolate, Irvine Scientific) and then washed twice with artificial human tubal fluid (HTF, Sperm Washing Medium, Irvine Scientific) to completely remove the residue of seminal plasma. After the second washing step, the sperms were resuspended with various culture media in centrifuge tubes at a concentration of approximately 10×10^6 sperms per mL and incubated at 37 °C with pH buffer Hepes until our imaging measurements. Three different culture media were used in this work: *(i)* Baseline medium, which only contained artificial HTF; *(ii)* suppressing medium I, which was prepared by mixing seminal plasma with HTF by a ratio of 1:9; and *(iii)* suppressing medium II, which was prepared by mixing seminal plasma with HTF by a higher ratio of 2:8. For all our imaging experiments except the time-traced ones (e.g., Fig. 5), the sperm suspensions were incubated for approximately 2–3 h. Right before lensfree imaging experiments, approximately 50–150 μL of the sperm suspension was put into a disposable observation chamber prepared by taping a laser-cut Acetal film (approximately 0.1–0.5 mm thick) between two pieces of No. 1 cover slips.

Dual-view and dual-color lensfree holographic imaging setup. The configuration of our imaging setup is illustrated in Fig. 1*A*. The observation chamber containing the sperm suspension is placed directly on top of the protective glass of a Complementary Metal—Oxide—Semiconductor (CMOS) image sensor (Aptina MT9P031STC, 5 megapixels, 2.2 μm pixel size, monochrome) creating a physical distance of approximately 0.8 mm between the bottom of the chamber and the top surface of the CMOS sensor active area. The sample suspension is simultaneously illuminated by two partially-coherent light sources with different central wavelengths placed at 45° with respect to each other (vertical one: 625 nm; oblique one at 45°: 470 nm). Both light sources were composed of light-emitting-diodes (LEDs, bandwidth approximately 20 nm) that were simply butt-coupled to multimode optical fibers (core size: 0.4 mm) with the fiber tips placed at a distance of approximately 10 cm from the sample chamber. Such a system, without utilizing any lenses or mechanical scanners, can simultaneously record in-line holograms of the sperms from two different viewing angles over a large field-of-view, e.g., >20 mm^2, while also significantly reducing unwanted noise terms such as speckle patterns, multiple reflection interference noise or cross-interference among sperms' holograms (1, 2). To capture the dynamics of the sperms with minimum motion blur, the electronic shutter of the CMOS image sensor was set to 5 ms for defining the integration time of each pixel. The FOV of the CMOS imaging platform (i.e., 24 mm^2) was digitally programmed into 16 regions-of-interest (ROIs), which were sequentially recorded at a frame rate of 92 frames per second (FPS) for continuous intervals of approximately 1–20 s each. The resulting video data were transmitted to a PC in real time through a gigabit Ethernet connection. To avoid the heating of the image sensor between tracking experiments, which might damage the sperms inside the observation chamber, a programmable power relay (connected to the PC through a USB interface) was used to cut off the power of the image sensor between video acquisitions. The ON-OFF cycle of the image sensor was carefully configured to maintain the observation chamber at 36–37 °C for several hours. A custom-designed LabVIEW program was used to coordinate the image sensor and the power relay for maintaining the temperature as well as to digitally scan over the 16 ROIs of the observation chamber. Scanning over 16 ROIs (with >1,600 lensfree holograms) and recording the trajectories of >1,500 sperms takes approximately 10 min for each semen sample. However, this acquisition time can be significantly reduced to approximately 30 s if external cooling is provided to prevent the overheating of the observation chamber.

Digital separation of sperm head's vertical and oblique lensfree projections. Because the spatial information of each sperm was encoded with different wavelengths at two viewing angles, only the reconstruction that is performed with the correct combination of distance (i.e., depth), angle, and wavelength can generate clear images of the sperms (Fig. S6). Since incorrectly reconstructed projection holograms of the sperms would only show up as weak background noise, the sperm head images projected in two different viewing angles at two different wavelengths can be isolated from each other although they were recorded at the same lensfree holographic frame. This provides an important solution to avoid confusing different projections of different sperms with each other, especially at high sperm densities, making our 3D tracking algorithm quite robust. Furthermore, without the need to record different viewing angles separately, this multicolor approach also simplifies our system, eliminating the use of pulsed light sources, high-speed digital cameras, and the synchronization between them.

We should also emphasize that the swimming sperm tails do not constitute a problem in our localization calculations since they are considerably narrower (≤0.6 μm) compared to the sperm head (approximately 3–4 μm wide) and exhibit very weak light scattering (3), which significantly decreases their holograms' strength compared to the sperm heads' holograms. This behavior is also confirmed by the fact that the swimming sperm tails do not appear in the reconstructed amplitude images of our lensfree system (Fig. S6).

Quantification of submicron 3D localization accuracy. Since the centroid coordinates of the vertical and oblique projections can be determined with an accuracy much better than the 2.2-μm CMOS pixel size (4), the dual-view holographic approach use can localize individual sperms in 3D with submicron accuracy. To shed more light on this, we conducted characterization experiments with 3 μm particles that are spread across flat glass surfaces, and the results of these experiments confirmed that we can provide a 3D localization accuracy of approximately 0.3–0.5 μm across a depth-of-field of approximately 2.7 mm (Fig. S7). Note that at larger depths (>3 mm) the signal-to-noise ratio of lensfree holograms relatively degrades, reducing our 3D localization accuracy. We chose 3 μm particles in these characterization experiments since they exhibit a contrast that is matched to human sperms in our reconstructed amplitude images.

Definitions of human sperm's 3D dynamic parameters. To quantify the 3D trajectories of human sperms with parameters that are compatible with the currently existing standards, we appropriately modified the parameters that are used by computer-aided

sperm analysis (CASA) systems (5), which can be summarized as below:

i. *Straight-line velocity* (VSL) is defined as the distance between the first and the last position points in the track segment of a sperm trajectory divided by the total duration of the track segment (unit: μm/sec).
ii. *Curvilinear velocity* (VCL) is defined as the sum of the distances between every two consecutive position points in a track segment divided by the total duration of the track segment (unit: μm/sec).
iii. *Linearity* is the ratio between straight-line velocity and curvilinear velocity (VSL/VCL) of a track segment (unit: none).
iv. *Amplitude of lateral head displacement* (ALH) is defined as twice the maximum displacement of a sperm head from its fitted moving axis in a track segment (unit: μm). It is directly related to the level of bending in the proximal region of the tail (6) (i.e., a larger ALH value corresponds to stronger bending).
v. *Beat-cross frequency* (BCF) is defined as the frequency that the sperm head moves across the middle plane of the "straightened" trajectory (unit: Hz). The middle plane is determined as the plane in the X_r-Y_r-Z_{ax} space that contains the central axis Z_{ax} and has the most frequent crossing-over of the sperm head (Fig. S8*C*). The value of BCF is in general sublinearly proportional to the beating frequency of the sperm tail and is roughly double the frequency of head wobbling (7).
vi. *Rotation speed* (RPS) is defined as the slope of the linear function that best fits the time evolution of the unwrapped rotation angle of a sperm head projected on the X_r-Y_r plane (unit: revolutions per second, r/sec). It represents how fast a helical track segment revolves around its moving axis and is roughly half of the value of the trajectory's beat–cross frequency.
vii. *Number of stable turns* (NST) is defined by multiplying the rotation speed of a sperm with the duration that a track segment maintains a small error (≤0.6 radians in this study) to the fitted linear function in its unwrapped angle (Fig. S8*E*); unit: none. The segment with a small angle error needs to be longer than one rotation cycle for being counted into the number of stable turns. NST represents how close the track segment is to a bended helix and we chose a value equal to or larger than 2 to qualify this track segment as a "helical sperm trajectory" (Fig. S2).

Automated processing of 3D sperm trajectory data. Data processing procedures including reconstruction of lensfree holographic images, localization of sperms' 3D centroids, tracking sperms' motion, and classification of their 3D swimming patterns were performed fully-automated with custom-designed Matlab programs. The typical computation time for automatic processing of, e.g., approximately 1,600 lensfree images from a single semen sample is approximately 2.2 h (using Matlab R2011a running on a PC with an eight-core Intel Core i7-930 2.80 GHz processor). Since most of these procedures are highly repetitive and parallelizable, this computation time can be significantly shortened (by >5-10X) (8) once our algorithms are further optimized for execution on graphics processing units (GPUs).

1. Mudanyali O, et al. (2010) Compact, light-weight and cost-effective microscope based on lensless incoherent holography for telemedicine applications. *Lab Chip* 10:1417–1428.
2. Greenbaum A, Sikora U, Ozcan A (2012) Field-portable wide-field microscopy of dense samples using multiheight pixel super-resolution based lensfree imaging. *Lab Chip* 12:1242–1245.
3. Su T-W, Erlinger A, Tseng D, Ozcan A (2010) Compact and light-weight automated semen analysis platform using lensfree on-chip microscopy. *Anal Chem* 82:8307–8312.
4. Su T-W, et al. (2010) Multiangle lensless digital holography for depth resolved imaging on a chip. *Opt Express* 18:9690–9711.
5. Mortimer ST (2000) CASA—Practical aspects. *J Androl* 21:515–524.
6. Mortimer ST, Schëväert D, Swan MA, Mortimer D (1997) Quantitative observations of flagellar motility of capacitating human spermatozoa. *Hum Reprod* 12:1006–1012.
7. Serres C, Feneux D, Jouannet P, David G (1984) Influence of the flagellar wave development and propagation on the human sperm movement in seminal plasma. *Gamete Res* 9:183–195.
8. Herraiz JL, et al. (2009) GPU acceleration of a fully 3D Iterative Reconstruction Software for PET. *2009 IEEE Nuclear Science Symposium Conference Record (NSS/MIC)* (IEEE), pp 4064–4067.

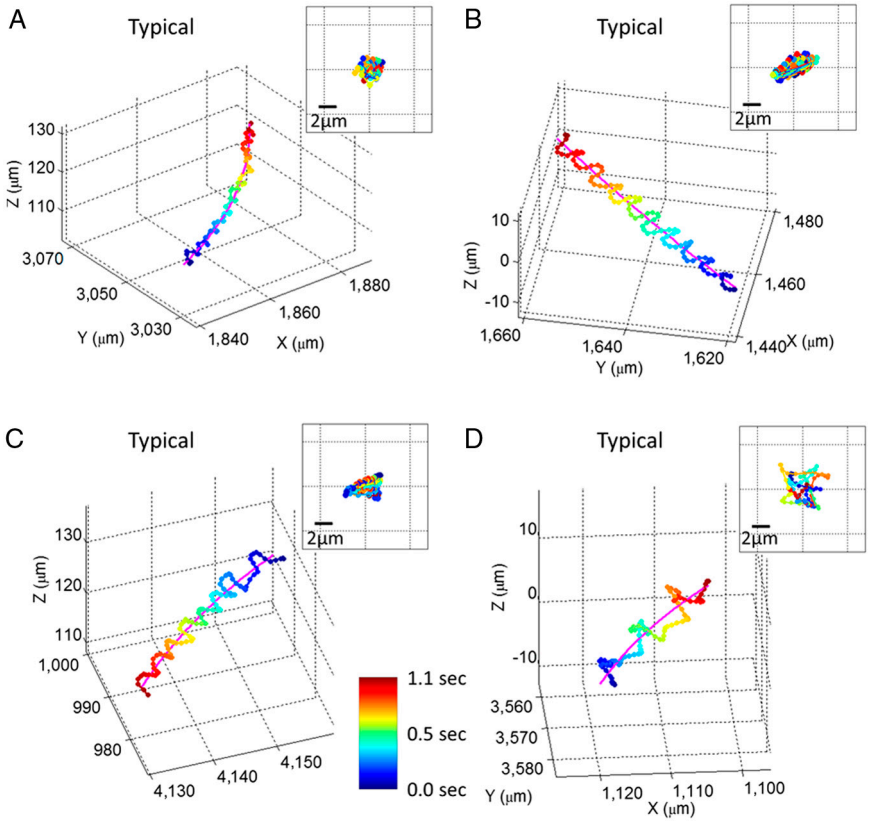

Fig. S1. Additional examples of human sperm typical swimming patterns. The inset in each panel is the front-view of the straightened trajectory of the sperm. The plane of $Z = 0$ is roughly aligned with the *Bottom* of the observation chamber. The time position of each track point is encoded by its color (see the color bar).

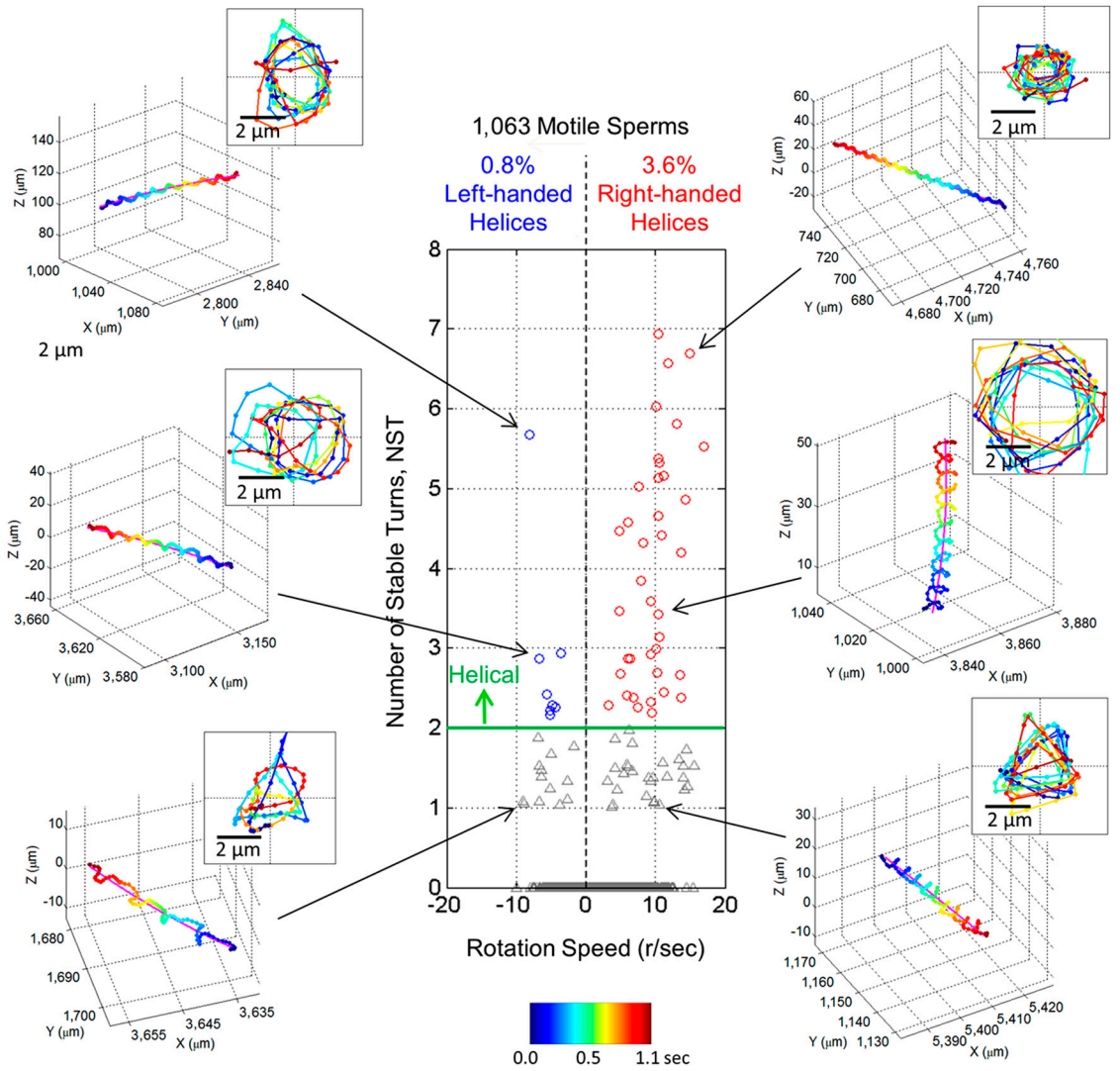

Fig. S2. Various examples of human sperm helical trajectories with different NST values. Within a given track period of approximately 1.1 s, a trajectory with more than two stable turns (NST $\geq$ 2.0) is considered a helical one (*Methods*). The plane of $Z = 0$ is roughly aligned with the *Bottom* of the observation chamber. The time position of each track point is encoded by its color (see the color bar).

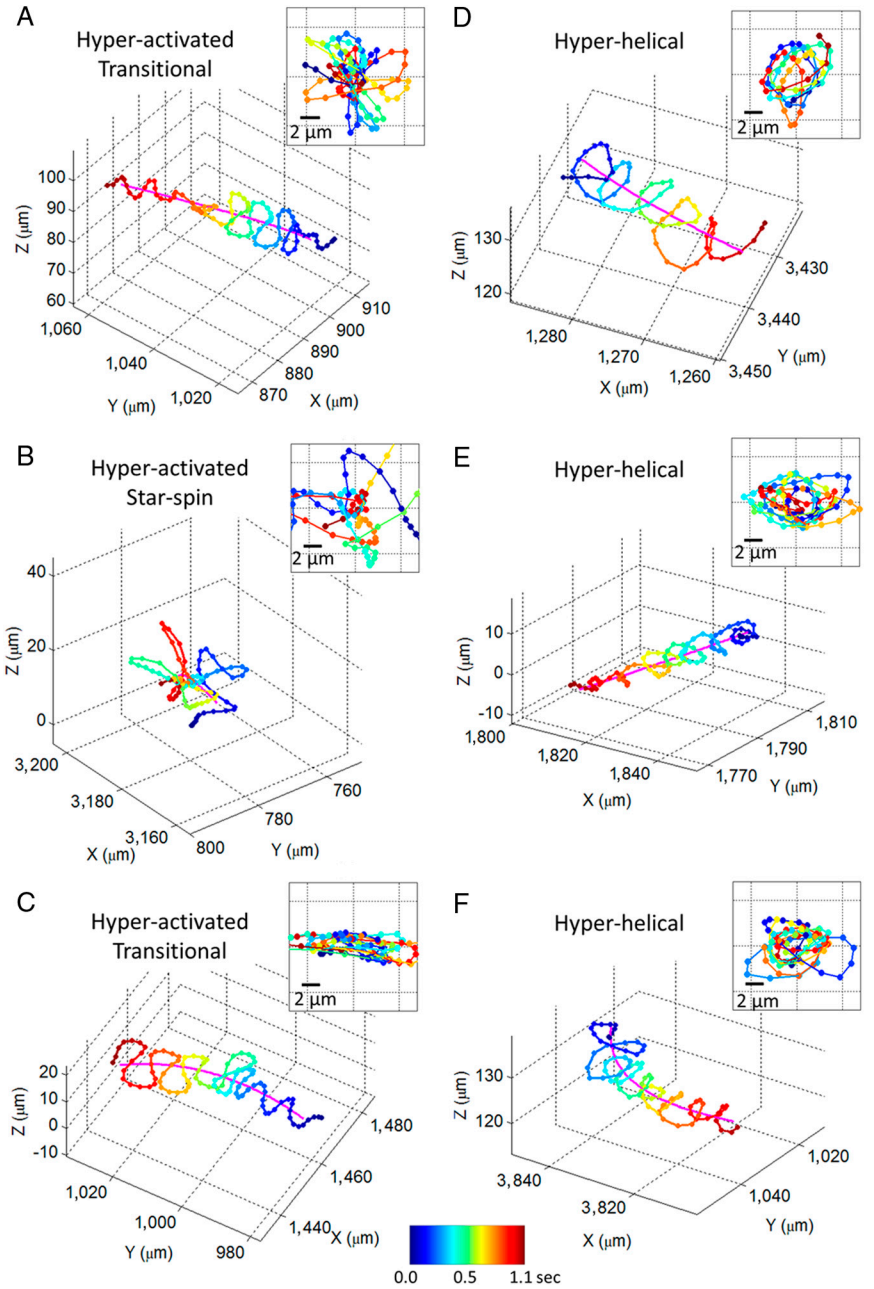

Fig. S3. Additional examples of hyperactivated (*A–C*) and hyperhelical (*D–F*) trajectories of human sperms. The inset in each panel is the front-view of the straightened trajectory of the sperm. The plane of $Z = 0$ is roughly aligned with the *Bottom* of the observation chamber. The time position of each track point is encoded by its color (see the color bar).

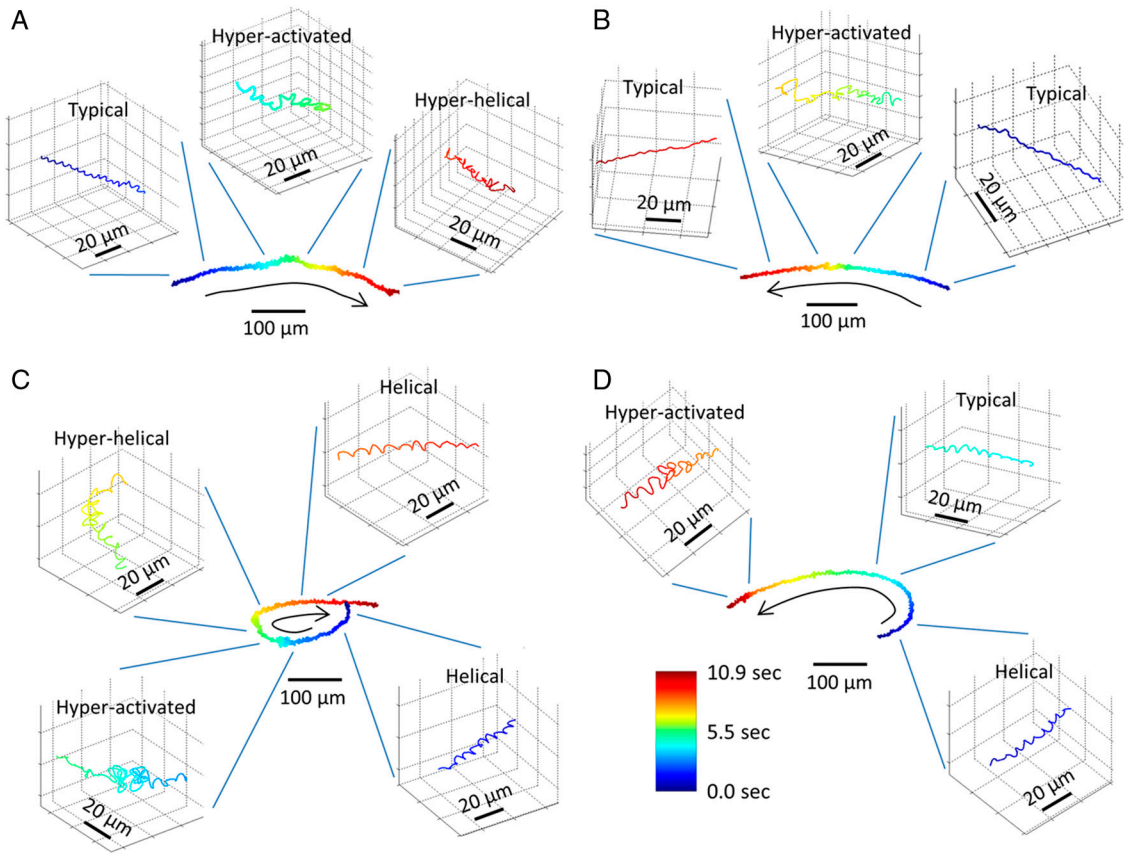

Fig. S4. Additional examples of human sperm trajectories showing the transitions among different 3D swimming patterns. The whole trajectories shown in (*A*), (*B*), (*C*), and (*D*) are each 10.9 s long, and the insets are digitally extracted segments of approximately 1.1 s. The time position of each track point is encoded by its color (see the color bar).

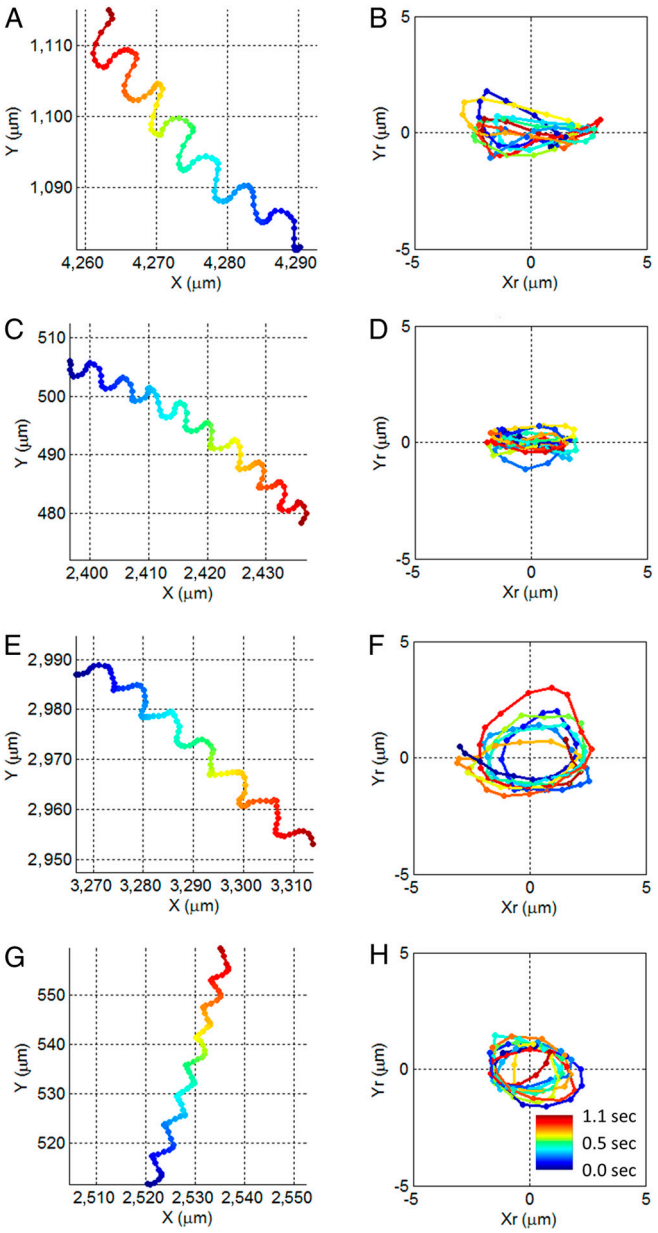

Fig. S5. 2D vs. 3D tracking of human sperms. (*A*) and (*C*) 2D tracking of two planar sperm trajectories. (*B*) and (*D*) The front views of the straightened 3D trajectories for (*A*) and (*C*), respectively (Fig. S8 and *SI Methods*). (*E*) and (*G*) 2D tracking of two helical sperm trajectories. (*F*) and (*H*) The front views of the straightened 3D trajectories for (*E*) and (*G*), respectively. As illustrated in this figure, unlike 3D imaging, 2D tracking of human sperms cannot differentiate planar and helical trajectories from each other.

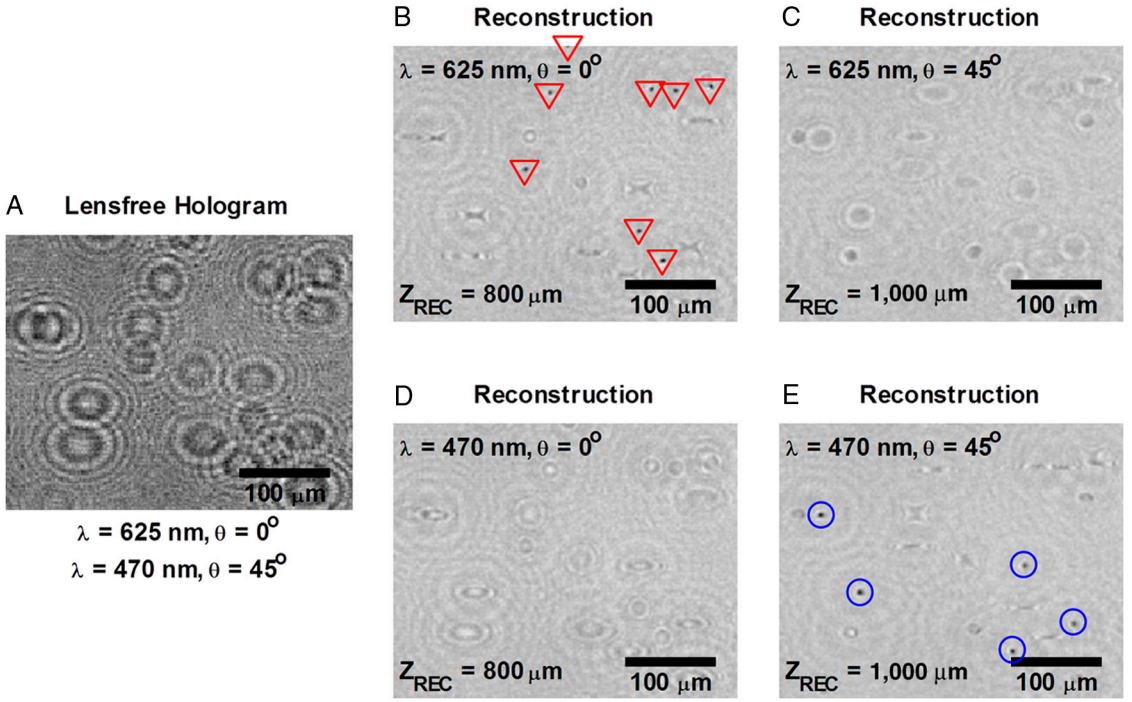

Fig. S6. Digital separation of the sperms' vertical and oblique lensfree projections through dual-angle and dual-color partially-coherent illumination. (*A*) A lensfree image showing several sperm holograms recorded with a red LED at the vertical angle and a blue LED at the oblique angle simultaneously illuminating the sample. (*B*)–(*E*) Lensfree images that were digitally reconstructed from the same region of interest shown in (*A*), but each with the conditions specified in its legends. The red triangles in (*B*) mark the successful detection of the vertical projections of the sperms, whereas the blue circles in (*E*) label the successful detection of oblique projections. Reconstruction with parameters that are not matched to the original illumination conditions would only create weak noise at the background as illustrated in (*C*–*D*). See Movie S6 for the time evolution of this lensfree hologram and its reconstruction images.

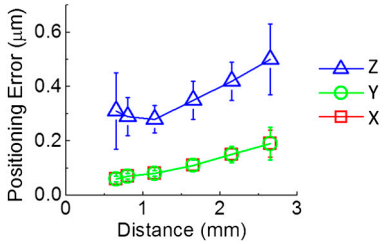

Fig. S7. The localization accuracy of the lensfree 3D tracking system as a function of the vertical distance from the sensor surface. The positional error was characterized by tracking microparticles (diameter: 3 μm) that are spread across flat glass surfaces and calculating the standard deviation of 3D positions for individual stationary particles. The vertical distance is defined by the separation between the localized object and the imaging plane of the CMOS sensor, which was adjusted by inserting glass slides of different thicknesses. Error bars define SD.

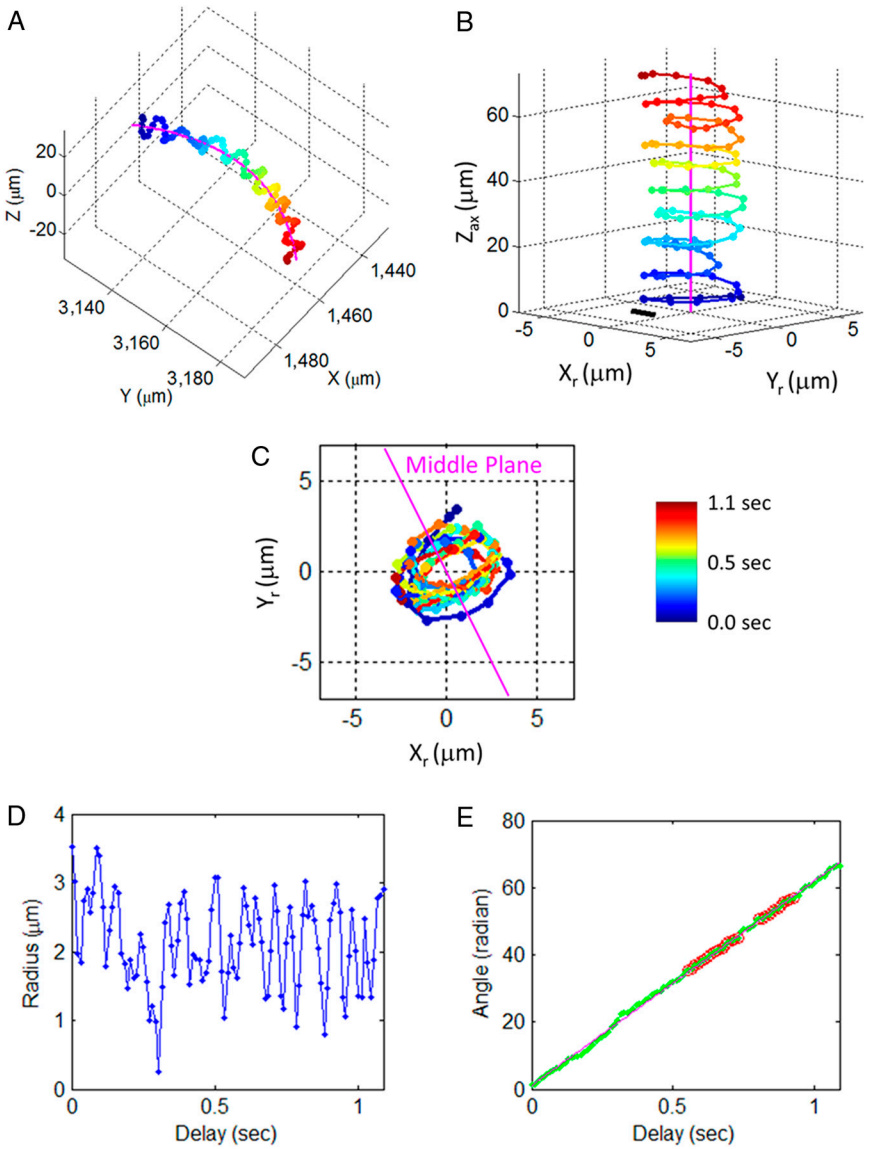

Fig. S8. Detection of a helical trajectory for a human sperm. (*A*) The original human sperm helix fitted with a parabolic line (magenta color) as its curved axis. (*B*) The same helix is straightened by replacing each point along a straight axis according to its relative displacement to the fitted axis (the magenta line). (*C*) The front view of the straightened helix shown in (*B*). The magenta line marks the middle plane that is used to measure the beat-cross frequency (*SI Methods*). The instantaneous radius (*D*) and angle (*E*) extracted from the lateral coordinates (i.e., X_r and Y_r) of the helix shown in (*C*). The angle in (*E*) is first unwrapped to eliminate possible 2π phase jumps and then fitted with a linear function (the magenta line) to match a stable rotation. Red circles on the magenta line in (*E*) mark the angular data points (the green dots) that lie within ± 0.6 radians from the fitted linear function.

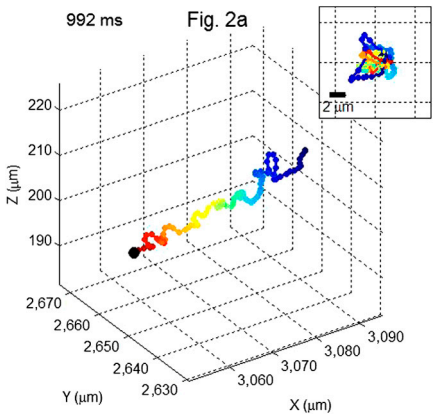

Movie S1. An example of human sperm typical swimming pattern.
Movie S1 (AVI)

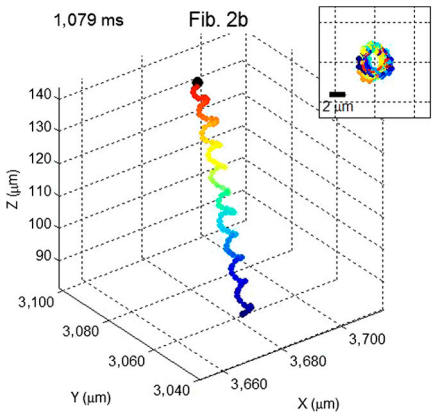

Movie S2. An example of human sperm helical swimming pattern.
Movie S2 (AVI)

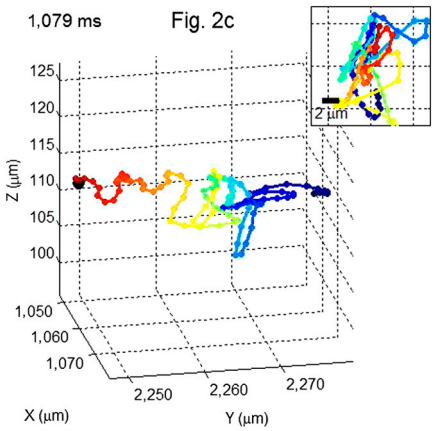

Movie S3. An example of human sperm hyperactivated swimming pattern.
Movie S3 (AVI)

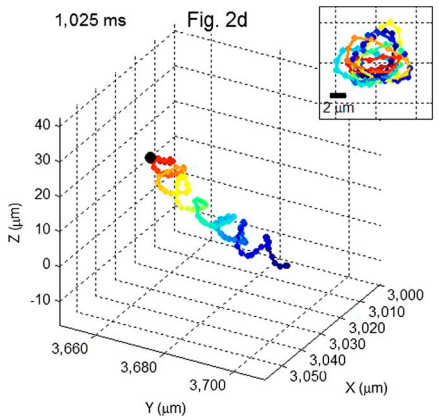

Movie S4. An example of human sperm hyperhelical swimming pattern.
Movie S4 (AVI)

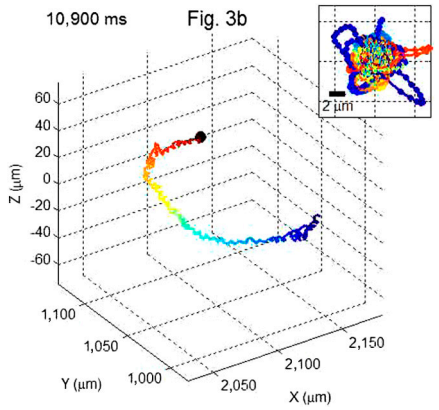

Movie S5. A 10.9-s-long trajectory showing the transitions between different swimming patterns of a human sperm.
Movie S5 (AVI)

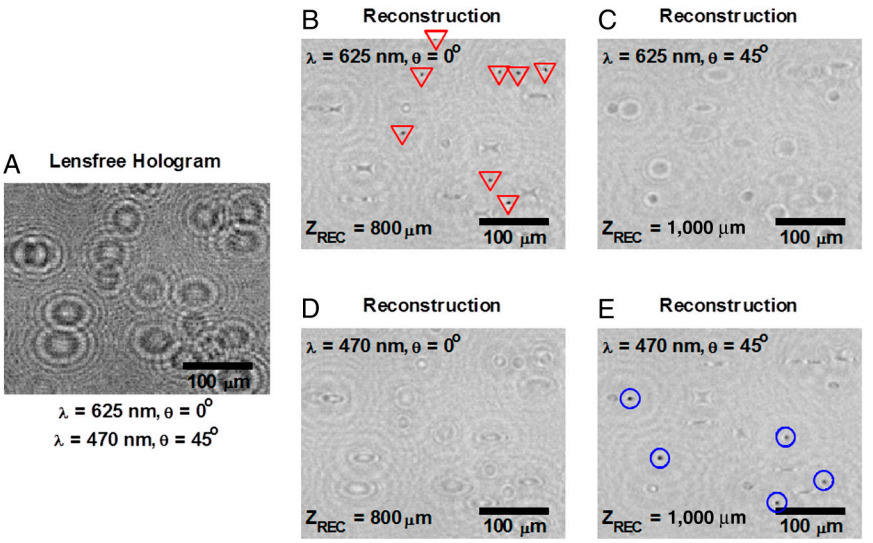

Movie S6. Digital separation of the sperms' vertical and oblique projections.
Movie S6 (AVI)

Table S1. The relative ratios of different swimming patterns

	Typical	Helical	Hyperactivated	Hyperhelical
Mean	**92.9%**	**4.4%**	**2.5%**	**0.2%**
Standard Deviation	(± 5.3%)	(± 1.5%)	(± 1.3%)	(± 0.2%)

These patterns were observed in 28 measurements of six semen specimens from different donors, containing 24,090 motile human sperms. The standard deviations listed in parentheses were obtained by calculating the deviation of each ratio observed across all the 28 measurements. These measurements were made in baseline medium (artificial HTF) after >2 h of incubation as described in *SI Methods*.

Table S2. The relative percentage of swimming pattern transitions (*From–To*)

		To			
		Typical	Helical	Hyperactivated	Hyperhelical
From	Typical	**85.1%** (± 8.1%)	**10.1%** (± 7.0%)	**4.8%** (± 4.1%)	**0.0%** (± 0.0%)
	Helical	**63.8%** (± 25.0%)	**30.0%** (± 22.1%)	**5.0%** (± 10.3%)	**1.3%** (± 3.6%)
	Hyperactivated	**57.7%** (± 31.3%)	**2.1%** (± 4.7%)	**30.9%** (± 28.6%)	**9.3%** (± 9.2%)
	Hyperhelical	**36.7%** (± 38.5%)	**13.3%** (± 30.7%)	**40.0%** (± 44.9%)	**10.0%** (± 30.3%)

The relative percentage of swimming pattern transitions (*From–To*) observed within 3,473 segments (each approximately 1.1 s long) of 656 human sperms trajectories (each approximately 5.5–10.9 s long). The standard deviations in parentheses were obtained by randomly dividing the 656 trajectories into 16 groups and calculating the relative percentage deviation of each transition across these groups.

Table S3. Typical values of various dynamic swimming parameters measured for motile human sperms

	Straight-line velocity (VSL) (μm/sec)	Curvilinear velocity (VCL) (μm/sec)	Linearity (VSL/VCL)	Lateral head displacement (ALH) (μm)	Beat-cross frequency (BCF) (Hz)
Mean	55.7	88.0	0.61	5.4	15.7
Standard Deviation	(± 24.9)	(± 28.7)	(± 0.21)	(± 2.9)	(± 5.1)

This table shares the same data as in Fig. 4 *A*, *B*, and *C* of the main text.

Table S4. Typical values of various dynamic swimming parameters measured for helical trajectories of human sperms

	Straight-line velocity (VSL) (μm/sec)	Curvilinear velocity (VCL) (μm/sec)	Linearity (VSL/VCL)	Helix diameter (μm)	Helix pitch (μm)	Frequency of rotation (RPS) (rev. per sec)
Mean	54.1	99.1	0.54	3.2	7.4	6.8
Standard Deviation	(± 21.0)	(± 30.3)	(± 0.11)	(± 1.0)	(± 2.0)	(± 4.6)

This table shares the same data as in Fig. 4 *D*, *E*, and *F* of the main text.